


Handbook
for
Generic Photonic IC Design

Editors: Meint Smit and Xaveer Leijtens

4-4-2026

 *Handbook for generic photonic IC design*, by the *Photonic Integration group*, Technische Universiteit Eindhoven, is licensed under a Creative Commons “Attribution-NonCommercial-NoDerivatives 4.0 International” license.

We traced the ownership of all figures used as far as we could. However, if you are a copyright owner and believe we used your work without permission, please contact us at coordinator@jeppix.eu.

Chapter 24

Optical Phased Arrays

MARCO GAGINO

Optical phased arrays (OPAs) are photonic integrated circuits (PICs) capable of forming an optical beam in free space thanks to the interference from multiple antennas and steering it by means of electrical signals. Due to the lack of moving parts and the integration of multiple optical components in millimeter-scale chips, OPAs can provide faster beam steering and have a higher reliability against vibrations compared to their mechanical counterparts (e.g., spinning-mirror and galvo-mirror scanners), micro electro-mechanical systems (MEMS), and liquid crystal spatial light modulators. OPAs are primarily used in light detection and ranging (LiDAR) sensing [284], optical wireless communication (OWC) [285, 286], biomedical applications [287, 288], as well as for imaging [289, 290] and 3D printing [291].

Optical phased arrays (OPAs)

LiDAR

Solid-state optical phased arrays have been designed in multiple photonic integration platforms that allow different wavelength ranges, leading to diverse applications. In the literature, one can find examples of OPAs operating in:

- visible range [292, 293, 294, 291, 295, 296]
- near infrared (NIR) [297, 293, 298]
- short-wave infrared (SWIR), including O-band, C-band, and 2 μm wavelength [299, 300, 301, 302]
- mid infrared (MIR) [303]

OPAs have been developed in many photonic platforms taking advantage of their individual strengths. Silicon photonics (SiPH) OPAs benefit from compact waveguides and electrical components that allowed the demonstration of large-scale optical phased arrays with up to 8192 antennas in a single chip (Fig. 24.1) [304, 307] and up to 49152 antennas through the combination of 24 OPAs in a super-reticle [305]. The number of electrically driven channels in an OPA is equal to the number of optical antennas and is proportional to the beam steering resolution, as will be shown in this chapter. An OPA with 1024 antennas was also demonstrated in a CMOS platform that monolithically integrated both photonic and electronic components [306]. Moreover, due to the compact waveguide dimensions, a wide field of view of (i.e., the beam steering range) of 180° was demonstrated with half-wavelength pitch waveguide arrays [308].

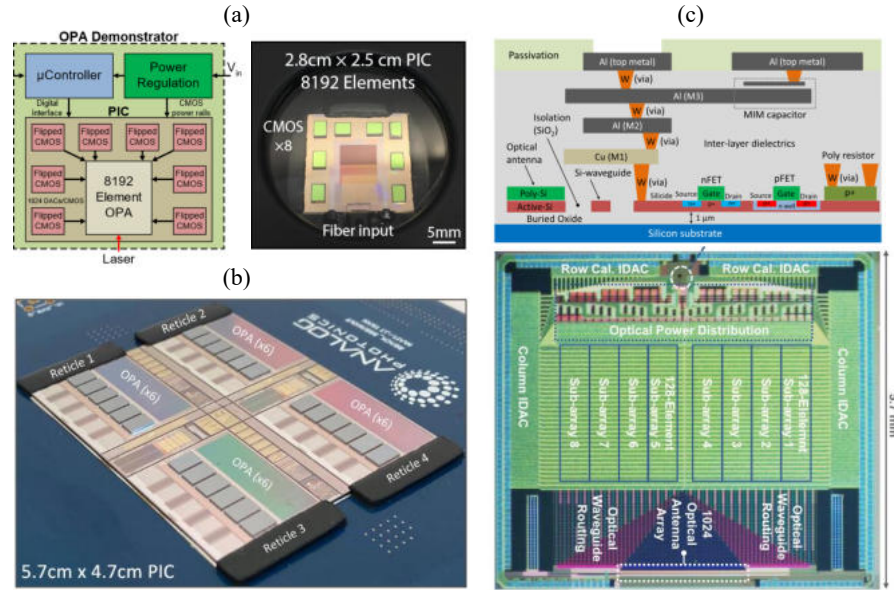


Figure 24.1: Silicon Photonics OPAs with large antenna count: (a) 8192-antennas OPA [304], (b) 49152-antennas super-cell OPA [305]. Both chips are LiDAR prototypes manufactured by Analog Photonics. (c) OPA-CMOS monolithic integration [306].

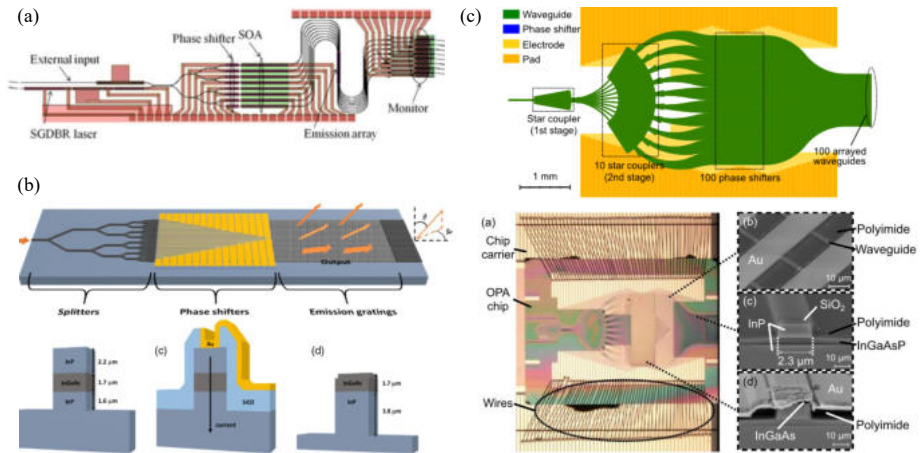


Figure 24.2: InP OPAs. (a) OPA with monolithically integrated laser source and grating-based 2D emitter [314]. (b) Mid-IR InP OPA [303] operating at $\lambda = 4.6\mu\text{m}$. (c) Largest scale InP OPA at the current state of art [315].

Multiple results have also been reported on Silicon Nitride (SiN) photonic platforms where two-photon absorption (TPA) losses are negligible and the damage threshold is higher than Silicon achieving hundreds of mW output optical power with Watt-level amplified input laser signals [309, 310, 292]. These results, coupled with the low propagation losses of the platform, are relevant for high-power optical beams for long-distance applications such as LiDAR and OWC. SiN also allows for a wide wavelength range of operation, and efficient and wide-aperture grating couplers for vertical emission and two-dimensional (2D) beam steering [311, 293, 312, 313].

The InP platform allows for the monolithic integration of the laser sources with the OPA beam steering circuit. Moreover, it allows on-chip amplification (for long-distance applications) and beam shape control through amplitude and phase control [316], as well as high-speed beam steering [317]. Finally, InP can operate in the SWIR wavelength range (O-band and C-band, up to $2\ \mu\text{m}$ [318]), and it is compatible with MIR wavelengths (Fig. 24.2b) [303, 319], thus allowing for LiDAR detection in a wide infrared wavelength range. InP optical phased arrays have been demonstrated with on-chip amplifiers and lasers, 2D vertical emission and beam steering through an array of grating couplers, and on-chip calibration through on-chip photodiodes [320, 321, 314] (Fig. 24.2a). The largest-scale InP OPA to date was demonstrated by Komatsu et al., with 100 channels, $5 \times 7\ \text{mm}^2$ footprint, 0.11° beam width, and 8.88° field of view (Fig. 24.2 c) [315]; a 16 ns response time of the phase modulators was measured.

In 2024, M. Gagino et al. [316] integrated multiple monolithically integrated semiconductor optical amplifiers (SOAs) in an InP OPA showing up to 21.5 dB net on-chip gain and up to 35.5 mW output power. These values represent, for the first time, a net on-chip gain instead of a loss that is typically of the order of $-10\ \text{dB}$ due to fiber coupling losses, emitting grating losses, waveguide propagation losses, and power splitting network losses. The PIC consists of an input booster amplifier, followed by a low-loss star coupler power splitter and 8 optical arms, each embedding an in-line amplifier and electro-optical phase modulators (Fig. 24.3). The publication also demonstrates that by adequately reducing the mutual heating (thermal crosstalk) of adjacent channels SOAs, it was possible to achieve up to 3.5dB higher gain. Moreover, control of both amplitude and phase in the OPA arms allowed to demonstrate a programmable shaping of the emitted beam. An increase was shown in the sidelobe suppression ratio (SLSR) up to 19.8 dB through the Gaussian apodisation of the emission profile and the generation of first- and second order Hermite-Gauss free-space beams. Finally, the same PIC (or an equivalent design) was employed to demonstrate high-speed wavefront shaping through scattering media [317], on-chip phase calibration [209], and the simultaneous control of both phase and gain by driving the SOAs exclusively [322], giving further examples of the advantages that InP brings to the functionality of optical phased arrays.

In the following sections of this chapter, the operation principle of OPAs will be described, and design considerations for their main working components will be laid down.

24.1 Operation Principle and Device Characteristics

An integrated OPA PIC is made up of several components, as shown schematically in Fig. 24.4. First, coherent light from a laser source (either integrated or fiber-coupled through an input waveguide) is split into N arms by a power distribution network (or power splitter). In each arm, light is carried by optical waveguides and a phase control element provides a tunable phase difference between neighboring arms. Finally, light is coupled into free space through optical antennas, which can be edge-emitting waveguides, as in the case of 1D OPA, or a 2D array of vertical-emitting grating antennas. In the most common implementation, the array of optical antennas is periodically arranged by a spacing d . A beam is formed in free-space in the direction θ_s where constructive interference between the optical antennas occurs. The beam can be steered by applying a phase shift in the arms so that the constructive interference condition is satisfied at different angles.

optical antennas

In the following sections, we take the example of a 1D optical phased array to discuss the optical properties of the beam formed in free space.

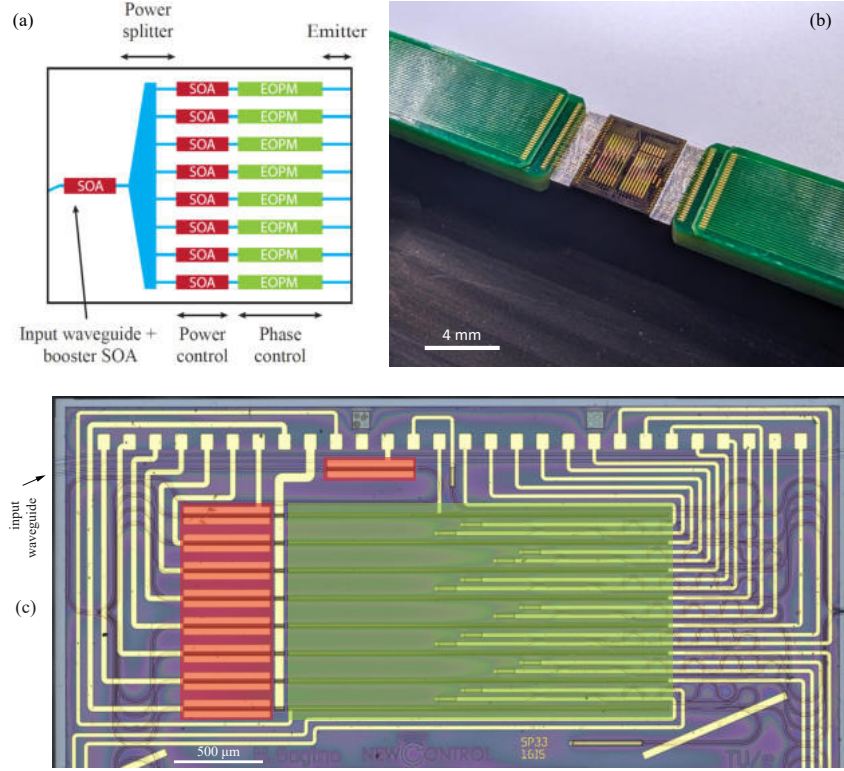


Figure 24.3: a) OPA circuit schematic (not to scale). (b) OPA assembly showing the PIC on an aluminium mount and wire-bonded to PCBs on each side. The chip contains two OPA circuits; the one used in this work is shown in the left half of the chip. (c) Microscope photograph of the fabricated OPA. The SOAs and EOPMs are highlighted in red and green respectively.

Beam forming

The coherent interaction between the light emitted by each OPA antenna results in an interference pattern similar to that generated by a N -slit aperture, described in first approximation by the Fraunhofer diffraction formula (Eqs. 24.1, 24.2, 24.3) [323, 324]. This model allows to calculate the far-field¹ intensity of the light $I(\theta, \theta_s)$ in a direction in space θ and for a steering angle θ_s as the product of an array factor $F(\theta)^2$ and an element factor $G(\theta)^2$.

$$I(\theta, \theta_s) = F(\theta)^2 G(\theta)^2 = \left| \frac{\sin\left(\frac{N}{2}(\delta(\theta) - \delta\phi(\theta_s))\right)}{\sin\left(\frac{1}{2}(\delta(\theta) - \delta\phi(\theta_s))\right)} \right|^2 \left(\frac{\sin \alpha(\theta)}{\alpha(\theta)} \right)^2 \quad (24.1)$$

$$\delta(\theta) = \frac{2\pi}{\lambda} d \sin \theta \quad (24.2)$$

$$\alpha(\theta) = \frac{\pi}{\lambda} w \sin \theta \quad (24.3)$$

¹The far-field is defined at a distance z beyond the Fraunhofer range $z > z_F = \frac{2D^2}{\lambda}$. D is the aperture of the antenna array and λ is the wavelength of the laser source.

The array factor F^2 (shown in blue in the plots of Fig. 24.5) depends on the number of antennas in the array (N) as well as the periodic spacing between them, i.e., the array pitch (d). For a spacing d that is smaller than half the wavelength ($d < \lambda/2$), a single beam is emitted in free space; its width depends on the total aperture of the arrayed antennas (Nd). For $d > \lambda/2$, on the other hand, the array factor results in periodic grating orders (or lobes) whose separation depends on d . In addition, multiple lower-intensity diffraction sidelobes appear on the sides of the main grating orders which arise from the discontinuity at the edges of the uniform power distribution in the near-field.

The element factor G^2 (shown in red in the plots of Fig. 24.5) describes the diffraction of light through individual antenna apertures, thus it depends solely on their geometry (i.e., the width of the antenna w). Due to its Gaussian-like shape, G^2 provides a windowing of the array factor that reduces the intensity of the high-order grating lobes with respect to the main lobe (i.e., the one pointing in the $\theta = \theta_s$ direction), as can be seen from the black curve of Fig. 24.5. The width of the optical antennas can thus be designed in such a way that the higher-order grating lobes are almost completely suppressed, although this will also result in a limited field of view.

This simple analytical model is useful for a straightforward validation of the impact of the pitch and waveguide width on the properties of the far-field. However, it assumes a uniform power distribution across the OPA arms and approximates the antenna near field as a uniform distribution. For a more precise representation of the element factor, one can approximate the individual waveguide modes at the edge of the PIC with a Gaussian function, or use simulation tools to precisely calculate the mode shape. Moreover, the power distribution across the arms can be given a different shape, which can be beneficial for the suppression of the diffraction order sidelobes of the optical beam. Finally, the spatial distribution of the antennas can be made aperiodic to suppress the grating orders of the envelope factor. A more detailed analytical model can be found in [324].

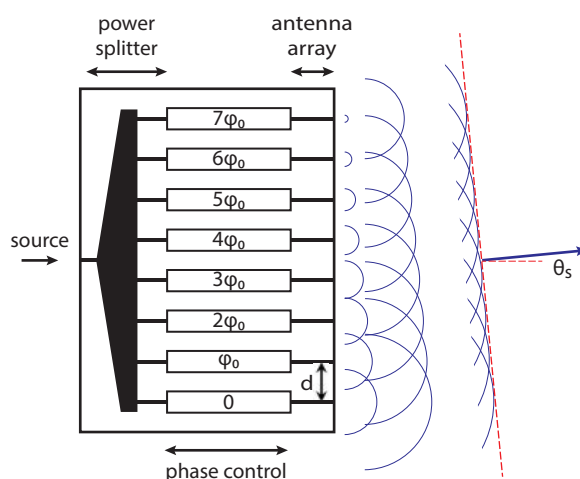


Figure 24.4: Schematic of an integrated optical phased array. An optical beam is formed in free-space through the interference of the beams emitted by each optical antenna. The phase front (red dashed lines) and steering direction (blue arrow) are indicated in the figure.

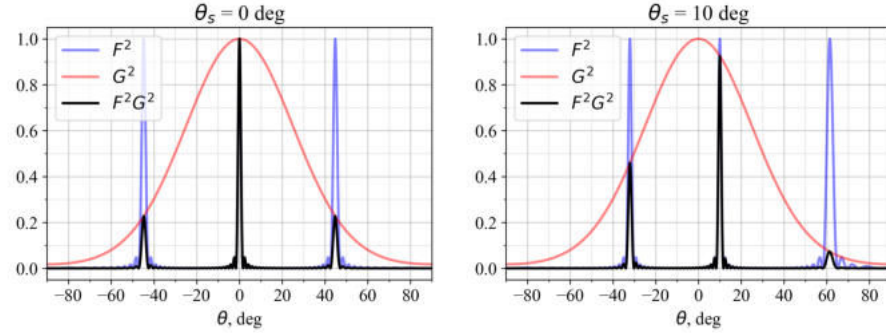


Figure 24.5: Far-field intensity plot showing the array factor and the element factor for an 8-channel array. The antenna width and spacing are $1.2\ \mu\text{m}$ and $2.2\ \mu\text{m}$ respectively; $\lambda = 1550\ \text{nm}$. (left) $\theta_s = 0$, (right) $\theta_s = 10^\circ$.

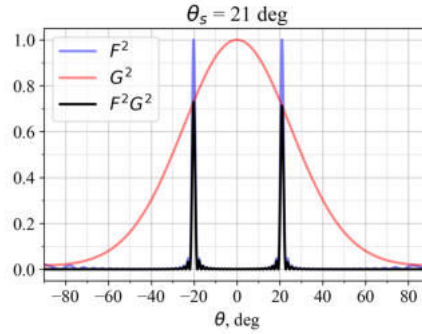


Figure 24.6: Far-field intensity plot at the aliasing condition ($\delta\phi = \pi$).

Beam steering direction

beam direction The beam steering direction θ_s is proportional to the phase difference $\delta\phi = \phi_0$ that is applied between adjacent arms through the phase control elements (thermo-optical or electro-optical phase shifters). The relation is shown in Eq. 24.4, where d is the spacing between the antennas.

$$\delta\phi(\theta_s) = \frac{2\pi}{\lambda} d \sin\theta_s \quad (24.4)$$

Field of view

Usually the antenna spacing d is $> \lambda/2$ due to the width and gap limitations for waveguides in the photonic integration platforms. This results in multiple grating orders emitted in free space. When the phase difference between adjacent arms is $\delta\phi = \pm\pi$, the first and second order grating lobes have equal intensity (also known in literature as the aliasing condition) as shown in Fig. 24.6. This case occurs at the angles $\pm \sin^{-1} \frac{\lambda}{2d}$, which determine the unambiguous angular scanning range, or field of view, of Eq. 24.5.

$$\text{FoV} = 2 \sin^{-1} \frac{\lambda}{2d} \quad (24.5)$$

Beam width

The beam generated by the OPA in the far-field (i.e., the main grating order) can be approximated by a Gaussian beam having a waist w_0 equal to the (half) total width of the emitter ($w_0 = Nd/2$). In this case, the angular beam width (or angular resolution) is defined by the Gaussian beam's divergence angle θ_{div} (Eq. 24.6), which is calculated by definition at $1/e^2$ of the peak intensity:

*Gaussian beam
angular beam
width
angular resolution*

$$\theta_{\text{div}} = 2 \frac{\lambda}{\pi Nd} \quad (24.6)$$

Often, this is translated to the full-width at half-maximum (FWHM), which is $\text{FWHM} = \sqrt{2 \ln 2} \theta_{\text{div}}$.

*full-width
half-maximum*

Emitter design tradeoffs

In an OPA with a periodic array of antennas, both the field of view and the angular resolution depend on the array spacing. Since applications like LiDAR typically require a large field of view and narrow beams, there is often a trade-off in the design of the two parameters. In the next section of this chapter, the main considerations to keep in mind when designing an OPA are described with a few examples. First, the optical crosstalk between adjacent edge-emitting waveguides is numerically simulated to understand the limitations in the OPA pitch, which defines the maximum obtainable field of view for a given integration platform. Then, an example of near-field and far-field calculations using simulated waveguide modes is provided. Two cases are considered: one where the far-field beam is generated by a uniform power distribution in the OPA arms (e.g., through an MMI splitting tree), and one with a beam generated by a Gaussian power distribution (for which a star coupler power splitter can be designed). With these simulation results, the advantages of employing a star coupler over the MMI splitting tree is described. Finally, simulations of optical losses of the star coupler and its power distribution across the OPA arms are reported, and the design tradeoff between the two is described.

24.2 Design of optical phased arrays components

24.2.1 Antenna spacing and optical crosstalk

In the design of OPAs, the field of view is typically limited by the aliasing condition that occurs in antenna arrays whose spacing d is greater than $\lambda/2$ (see Eq. 24.5). For this reason, the gap between waveguides and their widths are minimized in the design of OPA emitters. This can lead to optical crosstalk between adjacent edge-emitting waveguides, which results in variations of both the amplitude and phase distribution in the array output, and thus in an unpredictable far-field distribution. Thus, a study of the optical crosstalk is carried out to understand the limitations of the integration platform in minimizing the gap between the waveguide antennas.

The study of optical crosstalk also takes into account the the etch depth reduction that occurs in narrowly spaced InP waveguides, also known as the lag effect. This effect causes a lower mode confinement in the affected waveguides, which results in a stronger optical crosstalk between them.

Design a 1D OPA emitter following the steps given in problems *a-c*.

Problem a: Estimate the number of emitting antennas required in an OPA to achieve an image resolution of 512 points in a free-space steering range of $\pm 5^\circ$. $\lambda = 1.55 \mu\text{m}$.

Problem b: Calculate the angular resolution and the width of the emitter array under the conditions of the previous example.

Problem c: Under the conditions of the previous example estimate the width of the edge-emitting waveguides. Assume that when the main order is steered at 0° , the higher order grating lobes are suppressed by more than $1/e^2$ and approximate the waveguide mode to a Gaussian beam having waist equal to the waveguide width.

Solution a: Assuming that two beams are resolvable if their peak-to-peak separation is larger than their FWHM, we can define the image resolution as $N_{\text{res}} = \text{FoV}/\text{FWHM}$. For small steering angles, $\text{FoV} \approx \frac{\lambda}{d}$ (Eq. 24.5), and assuming a Gaussian beam is formed, $\text{FWHM} = 2\sqrt{2\log 2} \frac{\lambda}{\pi N d}$ (Eq. 24.6). Thus, $N_{\text{res}} = \frac{\pi}{2\sqrt{2\log 2}} N_{\text{ch}}$ and $N_{\text{ch}} \approx 0.75 N_{\text{res}}$. The image resolution N_{res} and the number of emitting antennas (or OPA channels) N_{ch} are almost identical in an array with uniformly spaced antennas.

Solution b: The FWHM beam width is $N_{\text{res}}/\text{FoV} = 0.02^\circ$. Given that the uniform separation of the antennas required for $\text{FoV} = 10^\circ$ is $d \approx \frac{\lambda}{\text{FoV}_{\text{rad}}} = 9 \mu\text{m}$, and that $N_{\text{ch}} = 384$, the total width of the emitter is 3.5 mm.

Solution c: The distance between the zero- and first-order grating lobes is equal to the FoV. To achieve a suppression of $1/e^2$ of the first-order grating lobes, the element factor must be such that its divergence is equal to the angular position of the lobe (Eq. 24.1), i.e., $\theta_{0,G} = \text{FoV} = 10^\circ$. Given that the waveguide geometry determines the element factor, and that $w_{0,G} = w_{\text{WG}}$, then $\theta_{0,G} = \frac{\lambda}{\pi w_{\text{WG}}}$, and $w_{\text{WG}} = 2.8 \mu\text{m}$.

Problem 24.1: Design of a 1D OPA.

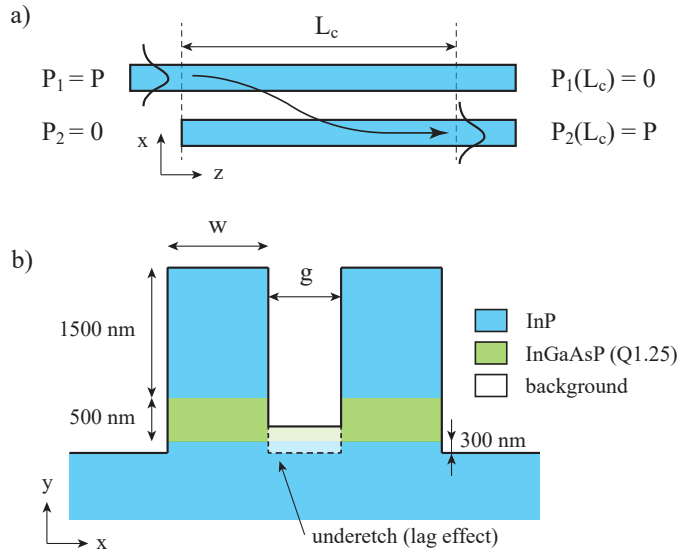


Figure 24.7: (a) Top view and (b) cross-section schematics of two neighboring waveguides exchanging optical power through crosstalk. In the example shown here, the power P is completely transferred from waveguide 1 to 2 at a length L_c .

It is worth mentioning that in the InP generic process, mode confinement for waveguides that are $\lesssim 1\mu\text{m}$ wide is unfeasible, making it impossible to achieve sub-wavelength arrays ($d < \lambda/2$) and thus 180° field of view with a periodic array of waveguides. Solutions to achieve close to 180° field of view with $d > \lambda/2$ have been reported in the literature (namely, sparse array of waveguides [299], wavefront shaping [288, 317], bidirectional OPAs [325]), as well as methods that rely on different platforms and crosstalk suppression methods to achieve $d \sim \lambda/2$ (waveguide superlattices [326], nanostructured arrays [327], periodically bending arrays [328]).

Simulating the optical crosstalk

The optical crosstalk between two neighboring parallel waveguides of width w and separated by a gap g (shown schematically in Fig. 24.7) can be simulated through finite-difference eigenmode (FDE) simulations of the coupled transverse-electric (TE) supermodes of the two-waveguide system, as shown in Fig. 24.8. The difference between the effective indices of the two coupled modes, $\Delta N = N_2 - N_1$, is related to the coupling length $L_c(r)$ for a given ratio of power transfer $r = P_2/P_1$ by Eq. 24.7. λ is the wavelength of the radiation in vacuum, P_1 is the total power in the TE mode launched into waveguide 1, and P_2 is the power coupled in the TE mode of waveguide 2 after an interaction length $L_c(r)$ (shown schematically in Fig. 24.7) [329].

$$L_c(r) = \frac{\lambda}{\pi\Delta n} \arcsin \sqrt{r} = \frac{\lambda}{\pi\Delta n} \arcsin \sqrt{\frac{P_2}{P_1}} \quad (24.7)$$

For the design of the OPA emitter, a coupling of 1% between two isolated waveguides will give an optical crosstalk of -20 dB which can be considered negligible in the array. In this case, the interaction length between the waveguides in the emitter array must

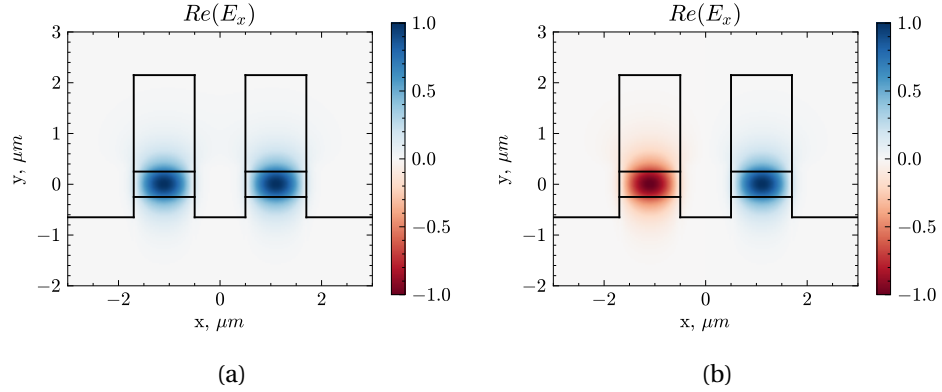


Figure 24.8: TE system modes (electric field amplitude) for two 1.2 μm wide deep-etched waveguides. The gap is 1 μm wide. (a) Symmetric mode. (b) Anti-symmetric mode.

be lower than the length at which 1% of power is transferred to the other waveguide, so $\arcsin \sqrt{P_2/P_1} = \arcsin \sqrt{0.01} \simeq 0.1$:

$$L_{\text{array}} < L_c(1\%) = 0.1 \frac{\lambda}{\pi \Delta n} \quad (24.8)$$

Lag effect

A reduced etch depth in the trench between two waveguides may occur due to the reactive ion etching lag effect [330, 331], as indicated in Fig. 24.7. This effect occurs due to the difficulty in transporting reactive species and ions into trenches with a high aspect ratio and extracting the reaction products [66]. In the OPA emitter array, this reduced etch depth causes a lower mode confinement, which results in a higher optical crosstalk between the waveguides. The FDE simulations described previously were thus performed taking into account the lag effect through the $(1 - l_{\%})$ parameter, which is defined as the percentage of the targeted etch depth t_{trgt} that is actually etched when there is lag effect, according to Eq. 24.9 (t_{lag} is the etch depth with lag effect). The $l_{\%}$ values were measured and reported by Bolk et al. [66] for an InP generic fabrication process. Its values are shown in Fig. 24.9 for different waveguide separations. For the simulations presented in this chapter, a generic InP platform is chosen, having a target etch depth measured from the top of the cladding of $t_{\text{trgt}} = 2.3 \mu\text{m}$.

$$t_{\text{lag}} = (1 - l_{\%}) t_{\text{trgt}} \quad (24.9)$$

Results of optical crosstalk and emitter design

Figure 24.10 shows the simulated 1% coupling length ($L_c(1\%)$) between two waveguides of varying width as a function of the gap between them. A deep-etch trench is assumed between the waveguides to maximize the confinement of the modes and minimize crosstalk, as shown in the schematic of Fig. 24.7. The simulations are performed at the central wavelength in the C-band, 1550 nm. The standard width for deep-etched waveguides in the InP generic platform, 1.5 μm , was used, as well as narrower waveguides. The background material surrounding the waveguides is air, al-

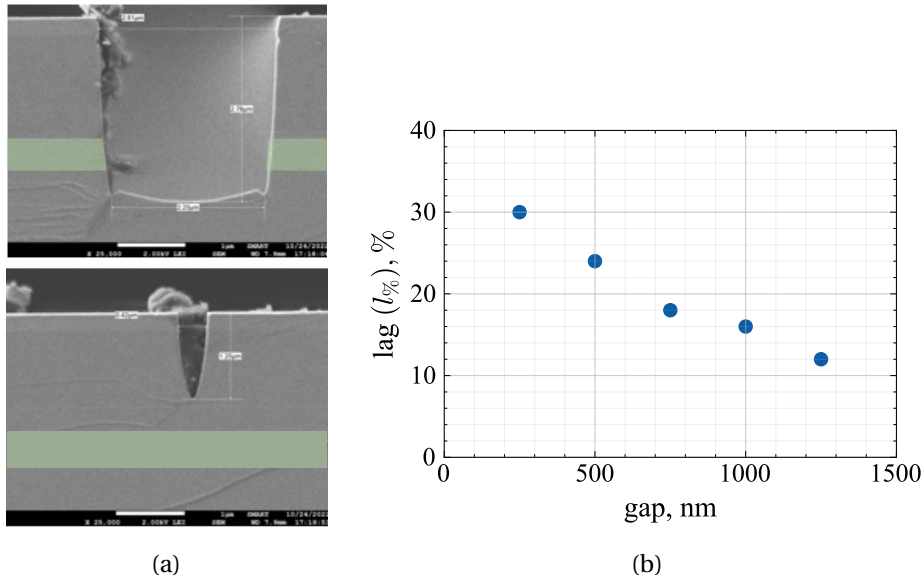


Figure 24.9: (a) SEM pictures showing lag effect between two closely spaced waveguides (courtesy of *SMART Photonics*). The etch depth reduction is worse for a smaller gap (lower picture). The waveguide core layer is highlighted in green. (b) Percentage of etch depth reduction due to the lag effect. The measurement data was reported in [66].

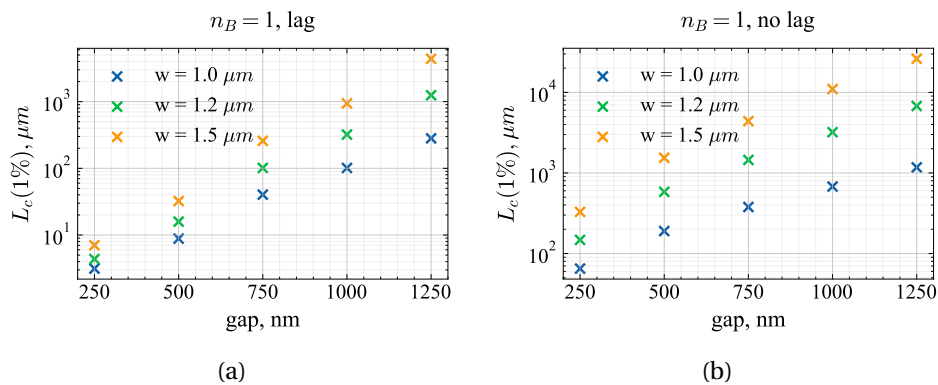


Figure 24.10: Coupling length for 1% of power transfer between two deep-etched waveguides. (a) Lag effect is considered in the simulation. (b) The waveguides are etched completely (no lag effect).

though similar results are obtained with a background material having a refractive index $n_B = 1.5$ (for example, representing the passivation and planarization layers).

As Fig. 24.10 shows, the lag effect is responsible for an order of magnitude worsening of the 1% coupling length compared to waveguides that are fully etched, due to the decreased confinement of the mode in the waveguides. In this chapter, a waveguide width of $1.2 \mu m$ and a pitch of $2.2 \mu m$ are chosen as a reference. These values ensure a $300 \mu m$ long array of parallel waveguides with less than 20 dB optical crosstalk between them. The pitch value corresponds to a beam steering field of view of 40° .

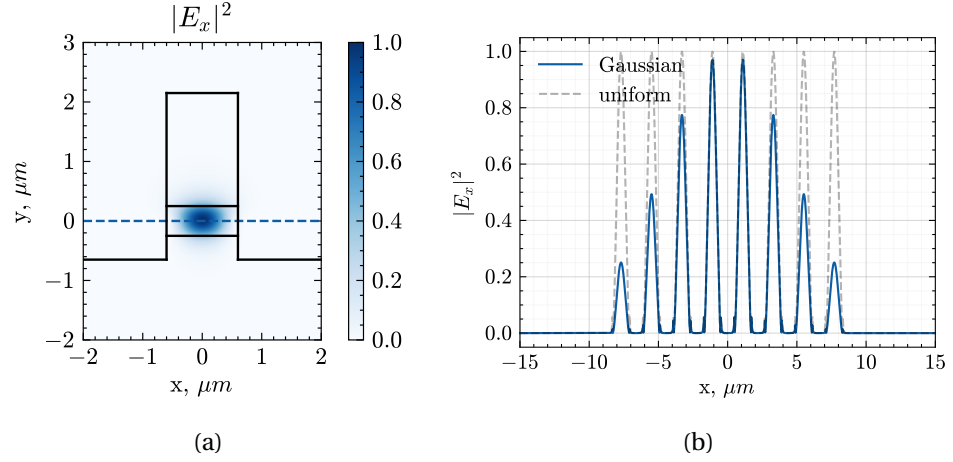


Figure 24.11: Electric field intensity (TE polarization). (a) Single waveguide mode, $w = 1.2 \mu\text{m}$. (b) Near-field of an 8-channel OPA with uniform and Gaussian distributions. 1D cross section along the $y = 0$ axis, at the center of the waveguide core. The waveguides pitch is $2.2 \mu\text{m}$.

24.2.2 Free-space emission

An OPA with uniform distribution of power across its antenna array, such as the one obtained with an MMI splitting tree, generates a far-field beam with strong diffraction *sidelobes* that deteriorates the optical signal to noise ratio. In the case of a star coupler power splitter, the near-field profile across the emitter antenna array can be approximated by a (truncated) Gaussian function. The resulting electric near field has a smoother transition to zero, compared to the square window of the uniform profile. For this reason, such OPAs give a stronger suppression of the diffraction *sidelobe suppression* (i.e., a higher sidelobe suppression ratio (SLSR)). However, this comes at the cost of a wider far-field beam [332, 333].

Since Eq. 24.1 describes a beam generated by a uniform near-field power distribution, a more accurate near-field model is given here. The OPA near-field can be constructed according to Eq. 24.10, which describes the electric field along the horizontal axis of the emitter.

$$E_{\text{NF}}(x) = \sum_{i=1}^N A_i M(x - x_i) e^{j\phi_i} \quad (24.10)$$

Under the assumption of negligible optical crosstalk between neighboring antennas, the electric field of the individual waveguide modes, $M(x - x_i)$ (where $|x_i - x_{i-1}|$ is equal to the array pitch d) can be combined through a summation along the horizontal direction. The electric field of the waveguide mode can be simulated in *Lumerical* FDE to accurately construct the near-field of the array (Fig. 24.11a). The amplitude distribution in the arms is defined by the terms A_i , while the phase difference between adjacent arms, $\delta\phi = \phi_i - \phi_{i-1}$, depends on the steering direction θ_s (Eq. 24.4). Figure 24.11b shows a comparison between two near-field profiles in an 8-channel array with $1.2 \mu\text{m}$ wide waveguides, separated by a pitch of $2.2 \mu\text{m}$. The uniform profile is compared to a Gaussian profile that has a non-uniformity $L_u = 6 \text{ dB}$ (defined as the ratio between the peak intensities in the outer and inner channels in the OPA near-field:

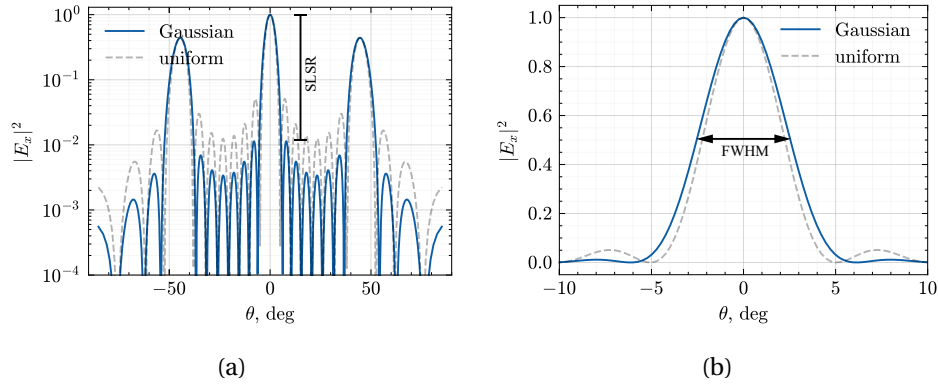


Figure 24.12: Far-field emission in log scale (a) and linear scale (b, zoomed in the main beam at 0° steering direction). The far-field generated by a uniform and Gaussian distributions are compared.

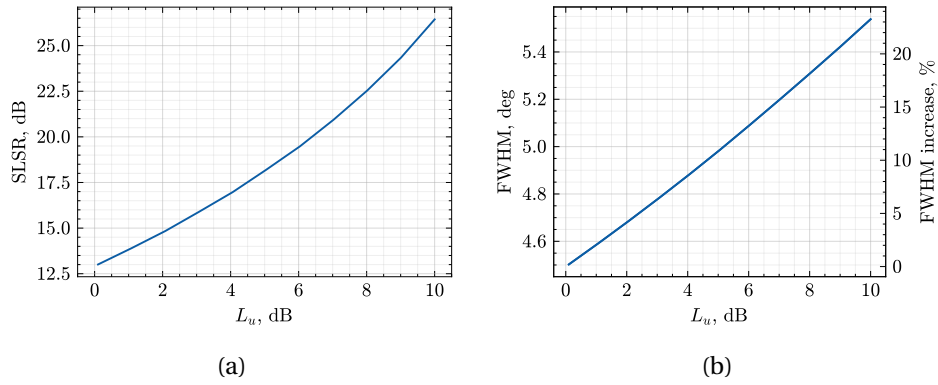


Figure 24.13: Far-field properties variations with the Gaussian beam uniformity, for an 8-channel OPA. $L_u = 0$ corresponds to the case of a uniform profile. (a) Sidelobe suppression ratio. (b) Beam width of the main lobe.

$$L_u = 10 \log_{10} \frac{A_{N/2}^2}{A_1^2} \quad (24.11)$$

The far-field is calculated through a Fourier transform of the near-field (Eq. 24.12), *far-field* which produces the intensity profile in the angular space shown in Fig. 24.12. The different beam properties (SLSR and FWHM) are highlighted for the two cases.

$$E_{FF}(\theta) = \text{FFT}(E_{NF}) \quad (24.12)$$

Fig. 24.12 shows the far-fields resulting from the 8-channel OPA near-fields having uniform and Gaussian profiles of Fig. 24.11. An improvement in the main beam SLSR from 13 dB (uniform profile) to 19.5 dB (Gaussian profile with $L_u = 6$ dB) can be observed, at the cost of an increase in FWHM from 4.5° to 5.1° .

A more generic case for the 8-channel OPA is shown in Fig. 24.13, where different values of Gaussian uniformity, L_u (Eq. 24.11), are simulated to quantify the variations of SLSR and beam width compared to a uniform profile (corresponding to $L_u = 0$). The

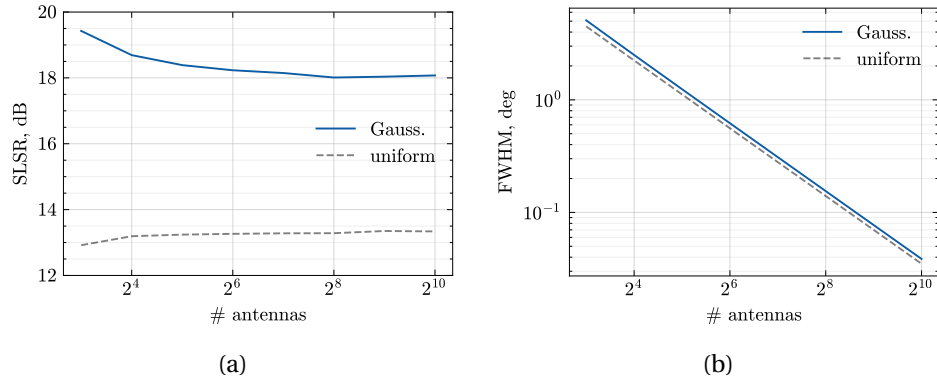


Figure 24.14: Comparison of far-field properties. The Gaussian distribution has an $L_u = 6$ dB. (a) Sidelobe suppression ratio. (b) FWHM beam-width.

SLSR is minimum (13 dB) for a uniform distribution, and can reach more than 25 dB for an array with Gaussian distribution having $L_u = 10$ dB. In this case, however, the FWHM is up to 25% wider compared to the beam with a uniform near-field profile. For a Gaussian uniformity $L_u < 6.5$ dB, the increase of FWHM is limited to 15%, while the SLSR can be as large as 20 dB. These considerations play a role in the design of the star coupler power splitter, in which the Gaussian uniformity L_u is one of the optimization parameters.

For a more realistic use-case the near-field and far-field intensities are simulated for OPAs with up to 1024 antennas, and the far-field SLSR and FWHM beam properties are calculated (Fig. 24.14). For OPAs having a Gaussian profile, the SLSR reaches a minimum of 18 dB with $N > 256$, whereas the uniform profile gives a stable SLSR of 13.3 dB. In order to achieve the 0.05° angular resolution necessary for long-range sensing applications with a pitch of $2.2 \mu\text{m}$ ($\text{FoV} = 40^\circ$), 720 OPA arms would be needed for a uniform near-field profile. Seventy additional channels (790 total) are required for an OPA with Gaussian near-field profile with $L_u = 6$ dB.

24.2.3 Power distribution in the PIC

In order to achieve power splitting in the N optical arms of an OPA, a power distribution network must be designed. In literature, the distribution of power is typically achieved with a splitting tree due to the compactness of the 1×2 MMI splitters that are employed [314, 303, 334]. *power splitting network* Moreover, this power splitting network can potentially guarantee the uniformity of both amplitude and phase in the OPA arms which simplifies the operation of the phased array, albeit in a limited operational bandwidth of the MMI. However, the non-idealities in the fabrication of the PICs make it unrealistic to obtain phase and amplitude uniformity across the arms, which makes phase-correction through a calibration step necessary to achieve beam forming. Another potential limitation of the MMI splitting tree is given by the optical losses of the building block, which could play a limiting factor in the OPA scalability when several hundreds of arms are targeted, such as for automotive applications. For example, we assume a typical MMI insertion loss of $IL_{\text{MMI}} = 0.5$ dB. As Fig. 24.15 shows, the total loss of the splitting tree, L_{TOT} , is $L_{\text{TOT}} = L_{\text{MMI}} \log_2 N$, which can result in 5 dB splitting loss for a 1024-arms OPA.

star coupler A star coupler power splitter can potentially achieve 1-2 dB optical losses independent

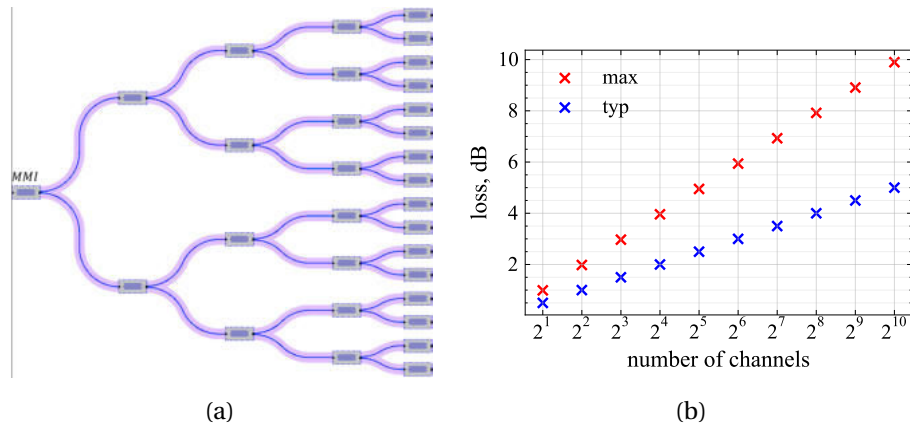


Figure 24.15: (a) Schematic of 1×2 MMI splitting tree dividing the power into 16 channels. (b) Optical losses associated with the power distribution network (for an MMI insertion loss of 0.5 dB and 1 dB in the blue and red plots respectively). The waveguide propagation losses are considered negligible.

of the number of arms in the array. Moreover, star couplers are compact, can operate in a wide wavelength range, and can provide a Gaussian power distribution in the arms (which benefits the SLSR), making them a better alternative to MMI splitting trees [335, 336, 315, 337, 338]. A model of the star coupler's dimensions, insertion loss, and power distribution across the arrayed waveguides is described in the next section.

Star coupler

A schematic representation of the star coupler building block is shown in Fig. 24.16.

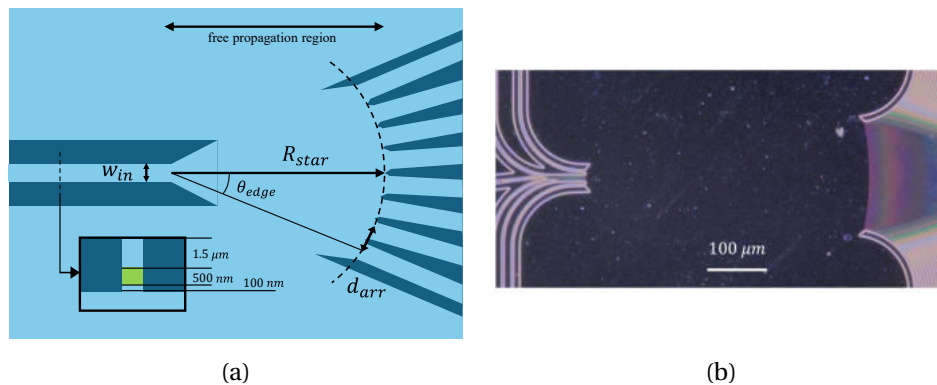


Figure 24.16: (a) Schematic top-view of an 8-channel star coupler. The cross section of a deep-etched waveguide is shown in the inset. (b) Microscope picture of a star coupler with multiple inputs and 104 arrayed waveguides.

An input waveguide of width w_{in} is followed by a free propagation region (slab waveguide, with a simulated effective refractive index $n_{eff} = 3.27$), where the mode is free to expand laterally. An array of N waveguides, shown on the right side of the schematic, is positioned around a circle of radius R_{star} with a period d_{array} along its circumference. The radius R_{star} approximates the phase front of the beam traveling through the free

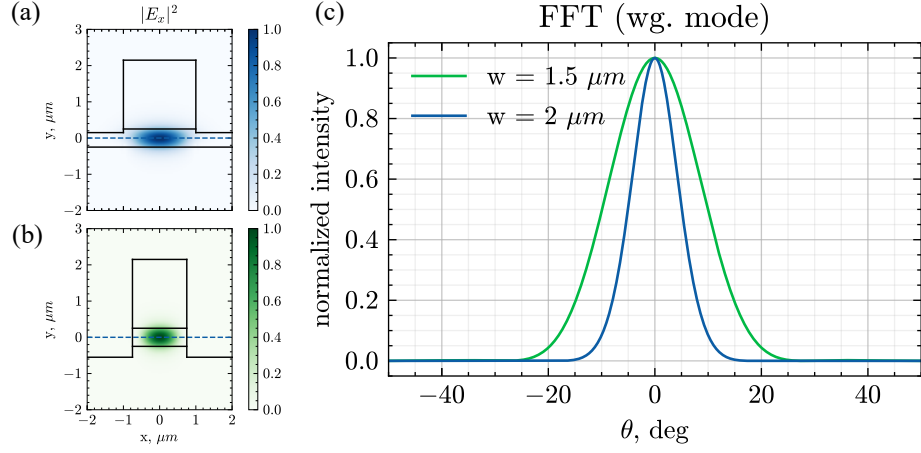


Figure 24.17: Input waveguide modes: (a) shallow-etched (2 μm wide), (b) deep-etched (1.5 μm wide). (c) Input waveguide mode in the free-propagation region.

propagation region at the input of the waveguide array.

To simulate the behavior of the star coupler, the electric field of the input waveguide mode $E_{\text{in}}(x)$ was simulated in *Lumerical* FDE (Fig. 24.17) for shallow (2 μm wide) and deep-etched (1.5 μm) waveguides. The input waveguide mode was propagated through the free propagation region using a Fourier transform $E_{\text{FPR}}(\theta) = \text{FFT}(E_{\text{in}}(x))$ (Fig. 24.17c) to calculate the intensity distribution in the angular space. This calculation is valid for a distance larger than the Fraunhofer limit, which depends on the input waveguide mode width. In order to calculate the power collected by each arrayed waveguide, the overlap integral between the waveguide modes, E_i (also simulated in *Lumerical*), and the mode in the free propagation region, E_{FPR} , is computed through Eq. 24.13, where x is the arc length of the circle of radius R_{star} . For the star couplers used in the OPAs presented in this thesis, the arrayed waveguides are standard 1.5 μm wide deep-etched waveguides because of their lower minimum bending radius compared to shallow-etched waveguides, which makes the star coupler more compact.

$$P_i = \frac{|\int E_{\text{FPR}} E_i dx|^2}{\int |E_{\text{FPR}}|^2 dx \int |E_i|^2 dx} \quad (24.13)$$

Two target parameters guide the optimization of the star coupler:

- The star coupler uniformity L_u (Eq. 24.14) is the power ratio between the inner ($P_{i=N/2}$) and outer ($P_{i=1}$) arrayed arms. Assuming that the mode in the free propagation region can be approximated by a Gaussian beam, the uniformity describes the Gaussian power distribution in the OPA arms.
- The star coupler insertion loss IL (Eq. 24.15) is the ratio between the power coupled in the arrayed waveguides (P_{arr}) and the power in the input waveguide mode (P_{in}).

$$L_{u,\text{dB}} = 10 \log_{10} \frac{P_{i=1}}{P_{i=N/2}} \quad (24.14)$$

$$\text{IL}_{\text{dB}} = 10 \log_{10} \frac{P_{\text{arr}}}{P_{\text{in}}} = 10 \log_{10} \sum_{i=1}^N P_i \quad (24.15)$$

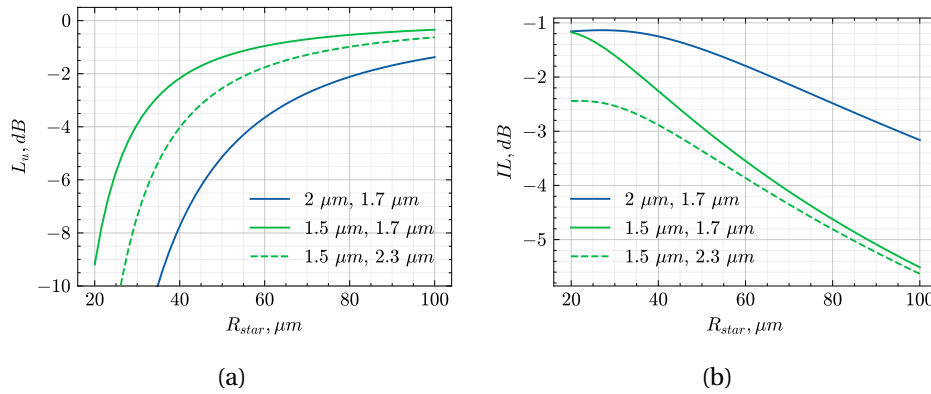


Figure 24.18: Gaussian power distribution in the star coupler (a) and its insertion loss (b). The legend indicates the input waveguide width (blue: $2 \mu m$ shallow waveguides, green: $1.5 \mu m$ deep waveguides) and the separation between arrayed waveguides: $d_{arr} = 1.7 \mu m$ (solid lines) and $d_{arr} = 2.3 \mu m$ (dashed lines). All arrayed waveguides are $1.5 \mu m$ wide and deeply etched. $N = 8$ for all curves.

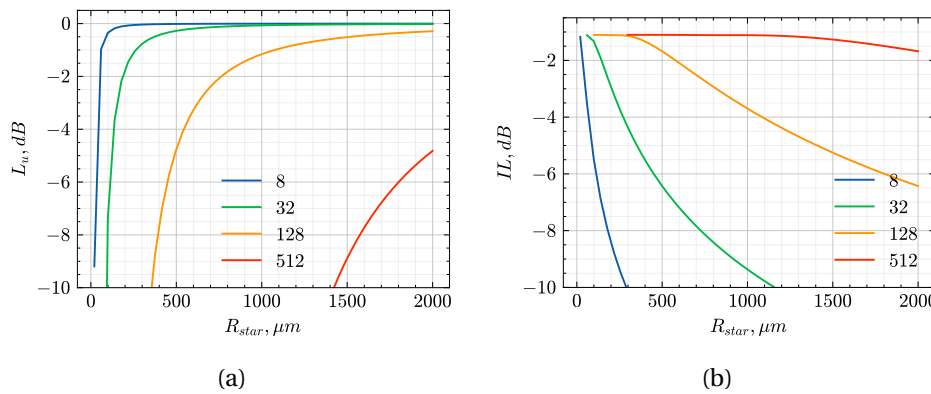


Figure 24.19: Gaussian power distribution in the star coupler arrayed waveguides (a) and its insertion loss (b). The legend indicates the number of arms in the array. The input and arrayed waveguides are standard $1.5 \mu m$ wide deep-etched waveguides. The pitch is $d_{arr} = 1.7 \mu m$.

By sweeping the star coupler radius R_{star} , one can optimize the matching between the mode in the free propagation region and the arrayed waveguide modes so that the insertion loss is minimized. This reduces the amount of power coupled in the edge waveguides and consequently the star coupler's uniformity (i.e., the absolute value of L_u increases).

The insertion loss and uniformity calculated with the method described above are shown in Fig. 24.18 as a function of the star coupler radius for different combinations of input (standard deep and shallow) and arrayed waveguides (standard deep). The gap between arrayed waveguides on the Rowland circle is ideally zero to minimize the losses associated with uncoupled light between waveguides. Due to the limited resolution of the fabrication processes involved in the definition of the waveguides, a non-zero minimum gap must be used. For a resolution of 200 nm , a minimum pitch of $d_{arr} = 1.7 \mu m$ when deep-etched waveguides are used must be guaranteed. In this case, the minimum star coupler insertion loss that can be achieved is close to 1 dB. A

range of losses in the 1-2 dB range can be achieved with Gaussian uniformities in the 3-6 dB range, and a radius R_{star} of a few tens of μm for an 8-channel star coupler. Figure 24.18 shows these results for a $2\ \mu\text{m}$ wide shallow input waveguide (blue curve) and for a $1.5\ \mu\text{m}$ wide deep waveguide (green solid line) and for a deep-etched array having a pitch of $1.7\ \mu\text{m}$. A third example is provided with an input deep waveguide ($1.5\ \mu\text{m}$ wide) and an array of deep waveguides having a gap of $800\ \text{nm}$ (pitch of $2.3\ \mu\text{m}$, dashed green curve), showing the degradation of the insertion loss when a larger gap is used.

Finally, the insertion loss and Gaussian uniformity are calculated for an increasing number of OPA arms to estimate the scalability of the building blocks for larger phased arrays and the results are shown in Fig. 24.19. Standard deep-etched input and arrayed waveguides were used with a pitch of $d_{\text{arr}} = 1.7\ \mu\text{m}$. Compared to a cascade of MMIs, whose loss is a function of the number of OPA channels, a star coupler with 6 dB uniformity can achieve a coupling loss $\text{IL} = 1.5\ \text{dB}$ regardless of the number of arrayed waveguides.

24.3 Conclusions

In this chapter, the optical phased array operation principle was described, and simple analytical expressions were given to estimate the shape and direction of steering of the beam in free-space. Furthermore, examples of state-of-the-art OPAs developed in multiple photonic integration technologies were described. The advantages of InP-based designs (i.e., monolithically integrated in-line amplification, high-speed phase modulation, and on-chip calibration to name a few) were highlighted with a few examples in literature. Designing these circuits requires navigating tradeoffs between field of view and angular resolution, while maintaining low levels of optical crosstalk between the multiple waveguides, which is further complicated by fabrication challenges like the lag effect. These concepts were explored in this chapter through design guidelines and numerical simulation methods. Moreover, the choice of the power distribution network is addressed, highlighting optical losses and the impact that the optical power distribution in the OPA arms has on the suppression of the diffraction sidelobes intensity. Ultimately, mastering these operational principles and component design techniques is essential for the development of high-performance, large-scale optical phased arrays.